Journal of Catalysis 278 (2011) 266–275

Contents lists available at ScienceDirect

Journal of Catalysis

journal homepage: www.elsevier.com/locate/jcat

Mesoporous Y zeolite with homogeneous aluminum distribution obtained by sequential desilication–dealumination and its performance in the catalytic cracking of cumene and 1,3,5-triisopropylbenzene

Zhengxing Qin [a], Baojian Shen [a,*], Xionghou Gao [b], Feng Lin [a], Baojie Wang [b], Chunming Xu [a]

[a] State Key Laboratory of Heavy Oil Processing; The Key Laboratory of Catalysis of CNPC; College of Chemical Engineering, China University of Petroleum, No. 18 Fuxue Road, Changping, Beijing 102249, PR China
[b] Lanzhou Petrochemical Center, Petrochemical Research Institute, PetroChina Company Limited, Lanzhou 730060, PR China

ARTICLE INFO

Article history:
Received 6 November 2010
Revised 16 December 2010
Accepted 17 December 2010
Available online 3 February 2011

Keywords:
Y zeolite
Ammonium hexafluorosilicate
Desilication
Dealumination
Mesopore
Catalytic cracking
Aluminum–silicon distribution

ABSTRACT

The aluminum–silicon distribution and mesoporosity of Y zeolites prepared by sequential NaOH desilication and ammonium hexafluorosilicate (AHFS) dealumination are compared with that of Y samples prepared via AHFS dealumination only. AHFS treatment led to severe non-uniform dealumination and substantial surface silicon deposition. Y samples obtained by sequential desilication and dealumination had substantially better dealumination uniformity and aluminum–silicon distribution. The mesopore formation in these zeolites is discussed in detail. The desilication creates defects in the framework of the parent NaY zeolite. These defects improve the intra-crystalline transport and induce mesopore formation during dealumination. The desilication- plus dealumination-treated zeolites showed higher initial activity and lower deactivation tendency in the case of 1,3,5-triisopropylbenzene cracking, and higher conversion rate of cumene than those zeolites modified by AHFS treatment only. These catalytic data indicate that the former could be a viable catalyst in the catalytic cracking of heavy hydrocarbons.

1. Introduction

As one of the post-synthesis approaches for the modification of the framework aluminum–silicon composition of zeolites, the fluorosilicate method has attracted great attention because of its unique characteristic of producing a zeolite that is free of non-framework aluminum. The dealumination reaction can be performed both in aqueous medium and in solid phase [1–6]. This technique has been successfully applied to a series of synthetic zeolites such as Y [1–8], mazzite and offretize [9], FAU/EMT intergrowths [10], ZSM-5 [11], Beta [12], MCM-22 [13], zeolite A [14,15], and mordenite [16]. In most cases, dealumination with ammonium hexafluorosilicate (AHFS) produces products with silica-rich surfaces. This was because dealumination by AHFS is a diffusion-controlled reaction [7,17]. Wang et al. further suggested that the surface silicon enrichment was due to the dealumination gradient and silicon deposition at the surface [18]. To prepare crystalline samples with high acidity with AHFS, Garralón et al. suggested that the aluminum extraction should be controlled [19]. Later, Ohsuna et al. showed that the surface silicon deposition reduced when FAU/EMT intergrowth was used as the parent material. Besides, some mesopores were created in the framework of such intergrowth-based products [10].

Despite all this progress, up to now no one has been able to prepare an AHFS-dealuminated Y zeolite with uniform aluminum–silicon distribution and mesopores of good accessibility. The distribution of aluminum strongly affects the catalytic performance of the zeolite [20,21]. The surface silicon enrichment leads not only to the reduction in surface acidity but also to the reduction in the utilization of the active sites inside the zeolite particles, which would be extremely disadvantageous for the catalytic applications of these surface silicon-rich zeolites. Cruz et al. have already found that, for an AHFS-dealuminated Y zeolite, it is the composition of the outer shell of the zeolite that controls the activity in the catalytic cracking of gasoil [7]. Although it has been reported that mesopores were created in the framework of an AHFS-dealuminated Y zeolite [10,22–26], little information is available regarding mechanisms of mesopore formation and evolution in this dealumination process.

The key to solve the surface silicon-rich problem is to improve the intra-crystalline diffusion of the reactant molecules during the AHFS dealumination process. The large size of the reactant molecules makes the reaction a diffusion-controlled process [7]. One possible approach to the problem of the confined intra-crystalline diffusion is to modify the porosity of the parent zeolite. According

* Corresponding author. Fax: +86 10 89733369.
E-mail address: baojian@cup.edu.cn (B. Shen).

0021-9517/$ - see front matter © 2010 Elsevier Inc. All rights reserved.
doi:10.1016/j.jcat.2010.12.013

to recent research, mesopore-containing zeolites can be prepared by NaOH treatment. The essence of this treatment is the rational use of the intrinsic nature of NaOH to selectively remove framework silicon. However, this mesopore-creating method has so far only been applied in the modification of high-silica zeolites, such as MOR [27,28], BEA [29], MFI [30,31], and ITQ [32]. When it comes to Y zeolite, whose framework silicon-to-aluminum ratio is low, the chance to introduce large amounts of mesopores in its framework through NaOH treatment would be remote, considering the previously established results that a high framework aluminum content inhibits the silicon extraction [33]. The original structure of the sodium carbonate-treated Y zeolite is essentially preserved [34]. Nevertheless, that framework silicon can also be selectively removed from the Y zeolite framework is undeniable, which means that defect sites will be created in the Y zeolite framework. The potential of these defects in assisting the intra-crystalline diffusion and mesopore formation has been underestimated. Introducing a functional group into open-framework materials that tunes the porosity will open new routes in framework engineering and in the fabrication of new types of materials [35]. From this perspective, the artificial defects in the framework of the Y zeolite framework left by silicon removal would be a very attractive "functional group" in facilitating the intra-crystalline diffusion and mesopore formation during AHFS dealumination.

When considering the further treatment of a pre-desilicated zeolite with AHFS, it is necessary to consider the resistance of the zeolite framework to the reactant used. After all, some silicon atoms have been removed from the zeolite framework. Therefore, the first purpose of the present research is to demonstrate that modified Y zeolite, with well-preserved crystallinity and substantially improved aluminum–silicon distribution and accessible mesoporosity, can be prepared via sequential desilication–dealumination. Another purpose is to explore how pre-desilication makes such a modification method possible. The catalytic cracking of cumene and 1,3,5-triisopropylbenzene (TIPB), with critical diameters of 0.68 and 0.95 nm, respectively, was investigated to characterize the catalytic performance of the prepared acidic samples.

2. Experimental

2.1. Desilication

The parent NaY zeolite used in this study was synthesized according to CN Patent ZL 200410097108.3 [36]. The phase purity of the crystallized product was checked by XRD. Desilication of the parent NaY zeolite was performed in 2–5 wt.% aqueous NaOH solution (cf. Table 1 for details). In a typical process, 1000 g of the aqueous NaOH solution was heated to 368 K, and then 100 g of the parent NaY zeolite was added to the hot solution. The resulting suspension was kept at 368 K for 1 or 3 h while stirring. Then, the slurry was suction-filtered and washed thoroughly with hot distilled water until a pH of 8.0. Products thus prepared were named ATY (Table 1).

2.2. Dealumination

The AHFS dealumination treatments were carried out as follows. First, the parent NaY and the ATY zeolites were converted into the NH_4^+-form (NH_4NaY and NH_4ATY) by three successive exchanges in 10 wt.% aqueous NH_4Cl solution. Then, 30 g of the NH_4^+-form zeolite was suspended in 300 g distilled water which was buffered at pH = 6 with ammonium acetate and heated to 338 K. To this buffered slurry, a predetermined amount of AHFS (Table 2) was added dropwise. The resulting slurry was maintained at 338 K for 1.5 or 3 h with stirring, then filtered, and washed thoroughly with hot distilled water. Based on the total amount and the way of addition of the reactant, the AHFS dealumination treatments are classified as "Case 1" and "Case 2" (Table 2). In "Case 1", a 8 wt.% aqueous AHFS solution (114 g) was added at a rate of 0.05 g AHFS per minute to the buffered slurry. The resultant slurry was maintained for 3 h with stirring. In "Case 2", a 4 wt.% aqueous AHFS solution (89 g) was added at a rate of 0.04 g AHFS per minute to the buffered slurry. The resultant slurry was maintained for 1.5 h with stirring, then filtered, and washed, and the same dealumination treatment was repeated once. Samples prepared from NH_4NaY zeolite and those from NH_4ATY zeolite under different reaction conditions were denominated FSY-1, FSY-2–1, FSY-2–2 and FS-ATY-1, FS-ATY-2–1, FS-ATY-2–2, FS-ATY-3, respectively (Table 2).

Table 1
The experimental conditions of the NaOH treatment[a].

Samples	Concentration of NaOH solution, wt.%	Time of treatment, h
ATY-1	2	1
ATY-2	4	1
ATY-3	5	1
ATY-4	5	3

[a] The reaction temperature is 368 K.

Table 2
The experimental conditions of the ammonium hexafluorosilicate (AHFS) treatment.

Samples	AHFS treatment conditions	Products
NH_4NaY	Case 1[a]	FSY-1
NH_4ATY-1	Case 1	FS-ATY-1
NH_4ATY-3	Case 1	FS-ATY-3
NH_4NaY	Case 2[b]	FSY-2–1[c], FSY-2–2[d]
NH_4ATY-2	Case 2	FS-ATY-2–1[c], FS-ATY-2–2[d]

[a] 8 wt.% aqueous AHFS solution (114 g), added at a rate of 0.05 g AHFS per minute, then maintained for 3 h with stirring.
[b] 4 wt.% aqueous AHFS solution (89 g), added at a rate of 0.04 g AHFS per minute, then maintained for 1.5 h with stirring, after a intermediate washing, the dealumination procedure was repeated once.
[c] The once-dealuminated semi-finished product of "Case 2".
[d] The twice-dealuminated samples of "Case 2".

2.3. Physicochemical characterization

X-ray diffraction patterns of the zeolites were obtained using a Bruker AXS D8 Advance X-ray diffractometer with monochromatized Cu Kα radiation (40 kV, 40 mA). Before the XRD measurements, the zeolite powder was dried at 393 K for 2 h in an oven and then kept in a closed vessel containing super-saturated aqueous $CaCl_2$ solution for 16 h to stabilize the moisture content of the zeolite. The relative crystallinity was estimated by comparing the peak intensities of the treated samples with that of the parent sample according to SH/T 0340–92. The total integrated intensities of the eight peaks assigned to the (331), (511), (440), (533), (642), (822), (555), and (664) reflections were calculated for the comparison. The scan range is from 15° to 35°, and the scan rate was 2°/min with a step width of 0.02°. The unit cell parameters of the parent NaY and ATY zeolites (α_{01}) were analyzed from the diffraction data using the Le Bail method [37]. For this purpose, the scan range is from 5° to 60°, and the scan rate was 1°/min with a step width of 0.02°. The unit cell parameters of the parent NaY, ATY, and the dealuminated zeolites (α_{02}) were determined from the position of the (555) reflection, using pure silicon (99.999 wt.%) as the internal standard for angle calibration ($2\theta = 28.443°$) according to SH/T 0339–92. The scan range is from 28° to 32°, and the scan rate was 0.05°/min with a step width of 0.02°. The framework Si/Al ratios of all the Y type zeolites involved in this work were obtained from the α_{02} by Eq. (1) [38], α_{02} taken in Å.

$$\text{framework Si/Al ratio} \frac{25.858 - \alpha_{02}}{\alpha_{02} - 24.191} \quad (1)$$

A Rigaku ZSX 100e X-ray fluorescence (XRF) spectrometer was used for the measurement of the bulk Si/Al ratio of the zeolites. X-ray photoelectron spectroscopy (XPS) measurements were performed on ESCALAB 250 (VG) using Al Kα ($h\nu$ = 1486.6 eV) radiation. Binding energies were referred to the C 1s at 285.0 eV. The aluminum coordination in the samples was characterized by ^{27}Al MAS NMR at a resonance frequency of 78.155 MHz. All spectra are calibrated to zero ppm using a liquid $Al(NO_3)_3$ reference. IR spectra of the hydroxyl region (3000–4000 cm^{-1}) were recorded on a Nicolet MAGNA-IR 560 spectrometer. Ten milligrams of the sample powder was pressed into a self-supporting wafer (1.33 cm^2) under 5 MPa pressure. Heat treatment of the wafers was performed in a home-made quartz cell (CaF_2 windows) at 673 K for 4 h in dynamic vacuum (10^{-2}–10^{-3} Pa). Subsequently, the sample was cooled to room temperature, and the spectrum was collected. Nitrogen physisorption measurements were performed at liquid-nitrogen temperature with a Micromeritics ASAP 2020 apparatus. Prior to the measurements, all samples were vacuum-degassed at 623 K for 5 h. The total surface area was determined by the BET method. The micropore and external surface areas as well as the micropore volume were calculated by the *t*-plot method. The pore size distribution profile and the mesopore volume were obtained by the BJH method with the N_2 desorption isotherm. Mercury intrusion experiments were performed on a Micromeritics Autopore IV 9500 apparatus to a final pressure of 228 MPa. Prior to measurements, samples were dried 2 h at 423 K.

The existence and the morphology of the mesopores were evaluated using a JEOL JEM-2100 electron microscope operating at 200 kV (point resolution: 0.19 nm). The particles were dispersed on a micro-grid without crushing or other mechanical treatments. NH_3-TPD of the catalysts was performed using a home-made apparatus, which consisted of a cylindrical quartz tube, a vertical well-controlled high-temperature furnace, and an Agilent 1790F gas chromatograph equipped with a thermal conductivity detector. A sample of 0.1000 ± 0.0002 g was charged in the quartz tube and heated at a rate of 10 K min^{-1} to 823 K for 120 min under He flow (1.5 l h^{-1}) before exposure to 100% NH_3 at 298 K for 30 min. The NH_3-TPD profile was recorded from 373 to 873 K at a heating rate of 10 K min^{-1} after removing weakly adsorbed NH_3 by heating the catalyst to 373 K under pure He flow (1.5 l h^{-1}).

2.4. Catalytic testing

Zeolite activity was determined with cumene and TIPB as the probe molecules, using a flow-type apparatus equipped with a fixed-bed reactor. Nitrogen was used as carrier gas at flows of 4.5–12 l h^{-1}. The catalysts were pressed binder-free and crushed to a particle size of 0.2–0.3 mm. The activation of the catalysts was carried out in situ with a rate of 4 K min^{-1} to the final temperature of 773 K and purged at this temperature with nitrogen for 3 h (flow rate = 4.5 l h^{-1}). In the case of cumene cracking, nitrogen saturated with vaporized cumene at 273 K was passed through the reactor (flow rate = 4.5 l h^{-1}), and the reaction temperature varied from 413 to 493 K. In the case of TIPB cracking, nitrogen saturated with TIPB at 353 K was passed through the reactor at 423 K (flow rate = 12 l h^{-1}). Reaction products were analyzed by an online gas chromatograph with flame ionization detector.

3. Results

3.1. Influence of desilication and dealumination on crystallinity and chemical composition of the zeolites

All the alkaline-treated zeolites still had good crystallinity (Table 3), indicating that the NaOH treatment had negligible damaging effect on the framework of the NaY zeolite. On the other hand, the unit cell parameters increased continuously as the NaOH concentration or reaction time increased. The $(SiO_2/Al_2O_3)_{XRD}$ ratio of the alkaline-treated zeolites decreased with increasing degree of treatment (Table 3). It has long been recognized that, in an alkaline solution, silicon will be selectively removed from a zeolite framework [27,34,39], as long as the zeolite treated is EFAL free [33]. No external aluminum sources were available under our conditions, and we checked with ^{27}Al MAS NMR that the parent NaY zeolite did not contain extra-framework aluminum. We therefore suggest that the removal of framework silicon is the sole reason for the increase in the unit cell parameter. As a result, some defects will be created in the framework of the alkaline-treated zeolites. These defects are more or less like the hydroxyl nests, which are known to be larger than an ordinary SiO_4 tetrahedron [40,41]. Hence, the larger the silicon removal, the more defect sites will be present in the ATY zeolite framework, and, as a result, the larger the unit cell parameter will be. Evidence showing the generation of defects in the framework of the desilicated zeolites comes also from the comparison of mass of zeolites before and after the alkaline treatment. Four alkaline-treated zeolites were obtained by alkaline treatment of the parent NaY with NaOH aq. solution of concentration 1 wt.%, 2 wt.%, 3 wt.%, and 4 wt.% for 3 h at 368 K. The corresponding mass loss of these alkaline-treated zeolites is 3.3 wt.%, 5.6 wt.%, 8.1 wt.%, and 12.9 wt.%. It is clear that the mass loss increases as the concentration of NaOH solution increases, suggesting that desilication does happen. Therefore, it is reasonable to state that defect sites are created in the framework of the treated samples as a result of the removal of parts of zeolite framework.

It is well known that the higher the SiO_2/Al_2O_3 ratio is, the more stable the structure of the zeolite will be. Therefore, it is possible that the crystallinity of the ATY-based products will deteriorate during AHFS dealumination due to the previous loss

Table 3
Crystallinity and chemical composition of the zeolites.

Samples	C/C_0[a], %	α_{01}[b], Å	α_{02}[c], Å	SiO_2/Al_2O_3 by XRD	Samples	C/C_0[a], %	SiO_2/Al_2O_3 by		
							XRD	XRF	XPS
Parent NaY	100	24.585	24.60	6.2	FSY-1	88	8.2	10.9	25.0
ATY-1	94	24.594	24.63	5.7	FSY-2–2	97	8.2	9.6	22.8
ATY-2	97	24.634	24.66	5.2	FS-ATY-1	86	8.1	9.6	16.4
ATY-3	93	24.654	24.69	4.8	FS-ATY-2–2	97	8.1	8.7	7.6
ATY-4	92	24.674	24.71	4.4	FS-ATY-3	85	8.0	9.1	10.9

[a] C/C_0: crystallinity of the zeolite relative to that of the parent NaY zeolite.
[b] Unit cell parameters obtained by analyzing the diffraction data using the Le Bail method.
[c] Unit cell parameters obtained by the silicon internal standard method.

of framework silicon. While the reaction conditions greatly influence the crystallinity of the final products (Table 3), in agreement with several other works [18,19,42], the FSY and FS-ATY zeolites prepared by the same conditioning AHFS treatments have comparable crystallinity (Table 3), both after mild and more severe dealumination (Cases 1 and 2 in Table 2). Besides, the $(SiO_2/Al_2O_3)_{XRD}$ ratios of all the FSY and FS-ATY zeolites are very similar. These data show clearly that, under our experiment conditions, the desilication has negligible effect on the crystallinity of the final products and on their framework silicon and aluminum composition. However, the XPS results indicate that there is a sharp difference in the surface SiO_2/Al_2O_3 ratios between the FSY and FS-ATY zeolites and between the final products prepared via the severe (Case 1) and mild (Case 2) dealumination treatments. For the FSY-1 zeolite, the surface silicon-to-aluminum ratio determined by XPS, $(SiO_2/Al_2O_3)_{XPS}$, is 16.8 higher than the framework silicon-to-aluminum ratio determined by XRD ($(SiO_2/Al_2O_3)_{XRD}$). The bulk silicon-to-aluminum ratio determined by XRF, $(SiO_2/Al_2O_3)_{XRF}$, which measures SiO_2/Al_2O_3 in the framework as well as in the amorphous layer, is 2.7 higher than the $(SiO_2/Al_2O_3)_{XRD}$ ratio (Table 3). The $(SiO_2/Al_2O_3)_{XPS}$ ratio of the FS-ATY-1 zeolite decreased to 16.4. This is a marked decrease compared to that of the FSY-1 zeolite. The $(SiO_2/Al_2O_3)_{XRF}$ ratio of the FS-ATY-1 zeolite decreased to 9.6, 1.5 larger than the corresponding $(SiO_2/Al_2O_3)_{XRD}$ ratio. For the FS-ATY-3 zeolite, the $(SiO_2/Al_2O_3)_{XPS}$ ratio decreased to 10.9, and the $(SiO_2/Al_2O_3)_{XRF}$ ratio further decreased to 9.1. XRD measures the framework composition, XPS measures the surface composition, and XRF measures framework plus extra framework. The closeness of these SiO_2/Al_2O_3 ratios in the case of the FS-ATY zeolites shows that treating the parent NaY zeolite with desilication before the AHFS treatment improves the aluminum–silicon distribution of the final dealuminated product.

Treating NH_4NaY and NH_4ATY zeolites under mild AHFS dealumination conditions (Case 2) also improves the aluminum–silicon distribution, while the degree of improvement largely depends on the situation. In the case of the FSY-2–2 zeolite, the $(SiO_2/Al_2O_3)_{XPS}$ ratio decreased from 25.0 to 22.8 only, which is still 14.6 higher than its $(SiO_2/Al_2O_3)_{XRD}$ ratio (Table 3). In the case of the FS-ATY-2–2 zeolite, however, a clear improvement in aluminum–silicon distribution occurred. The $(SiO_2/Al_2O_3)_{XRD}$ ratio of this zeolite is 8.1, and the $(SiO_2/Al_2O_3)_{XPS}$ ratio is 7.6. Clearly, pre-desilication is more effective than the modification of AHFS dealumination conditions in governing the aluminum–silicon distribution of the final products, in view of the fact that the $(SiO_2/Al_2O_3)_{XPS}$ ratio of the FSY-2–2 zeolite is 6.4 higher than that of the FS-ATY-1 zeolite. The combination of these two works even better in modifying the distribution, as exemplified in the case of the FS-ATY-2–2 zeolite. Previous studies showed that the difference between the framework SiO_2/Al_2O_3 ratio and the SiO_2/Al_2O_3 ratio of the outer surface is a sign of dealumination gradient and silica deposition [18]. The traditional AHFS dealumination treatment is often beset by deposition and inhomogeneous dealumination problems. If the same applies for our FSY-type zeolites, then one may suggest that these problems can be eliminated by a combined use of pre-desilication and AHFS dealumination.

3.2. Influence of desilication and dealumination on zeolite structure

3.2.1. N_2 sorption

The effect of desilication on the pore structure of the ATY zeolites can be clearly seen in the N_2 sorption isotherms (Fig. 1). The slopes of the isotherms of the ATY zeolites are larger than that of the parent NaY zeolite. This means that the surface adsorption capacity of the ATY zeolites is higher. The pore size distribution (Fig. 2) shows that there is a wide range of pore sizes. Increasing

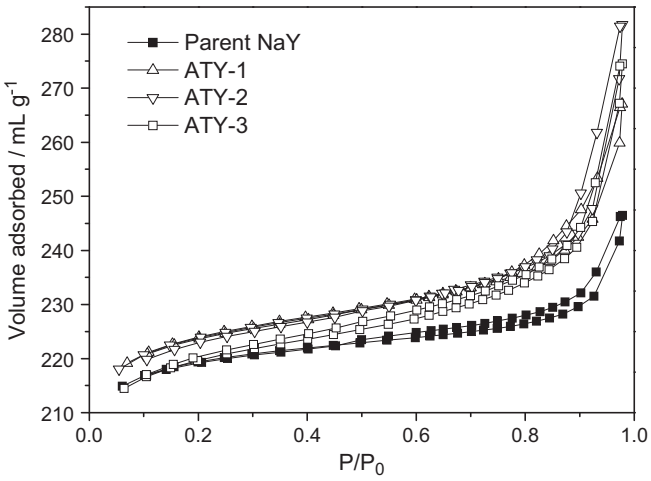

Fig. 1. N_2 adsorption and desorption isotherms of the parent NaY and ATY zeolites.

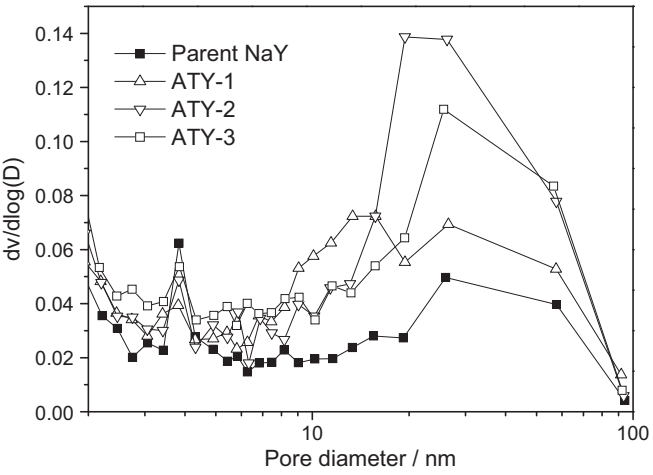

Fig. 2. Pore size distributions of the parent NaY and ATY zeolites.

the NaOH concentration results in an increment in the volume of the mesopores (Table 4). On the other hand, the formation of these mesoporous defects is not accompanied by any detectable debris in the micropores, since all the ATY zeolites have at least an equally high micropore volume as the parent NaY zeolite (Table 4).

After the AHFS treatments, all the samples dealuminated under the same conditions show comparable residual micropore volume (Table 4). Moderating the severity of the dealumination condition modified the preservation of the microporosity. These N_2 sorption results confirm the XRD data (Table 3) that the pre-desilication has no detrimental effect on the micropore system of the final products. On the other hand, all the dealuminated zeolites showed some increase in mesopore volume compared to their respective sodium-form precursors (Table 4), suggesting that some mesopores are created in the zeolite framework. These mesoporous structures all show a bimodal pore size distribution (Figs. 3–5). For the FSY-1 and FS-ATY-1 zeolites, two peaks appear at ca. 4 and 8 nm (Later, it will be shown that the 4 nm peak is an artifact). For the FS-ATY-3 zeolite, the two peaks appear at ca. 9 and 26 nm (Fig. 3). Treating NH_4NaY and NH_4ATY zeolites with AHFS of a lower concentration (Case 2) increases the micropore volume of the final products (Table 4), while the pore size distributions of these

Table 4
The surface area and pore volume data of all the Y type zeolites involved.

Samples	S_{micro}[a], $m^2\ g^{-1}$	$S_{external}$[b], $m^2\ g^{-1}$	V_{micro}[c], $cm^3\ g^{-1}$	V_{meso}[d], $cm^3\ g^{-1}$	V_{Hg}[e], $cm^3\ g^{-1}$
Parent NaY	680	18	0.33	0.06	–
ATY-1	677	31	0.34	0.09	–
ATY-2	683	31	0.33	0.11	–
ATY-3	659	35	0.33	0.11	–
FSY-1	549	54	0.27	0.15	0.07
FSY-2–1	643	37	0.32	0.08	–
FSY-2–2	617	56	0.30	0.12	0.08
FS-ATY-1	559	61	0.27	0.17	0.10
FS-ATY-2–1	678	40	0.34	0.13	–
FS-ATY-2–2	648	55	0.32	0.17	0.17
FS-ATY-3	557	58	0.27	0.19	0.19

[a] *t*-plot micropore surface area.
[b] *t*-plot external surface area.
[c] *t*-plot micropore volume.
[d] BJH mesopore volume.
[e] Mercury intrusion volume (6–100 pore size range). "–" no data were collected.

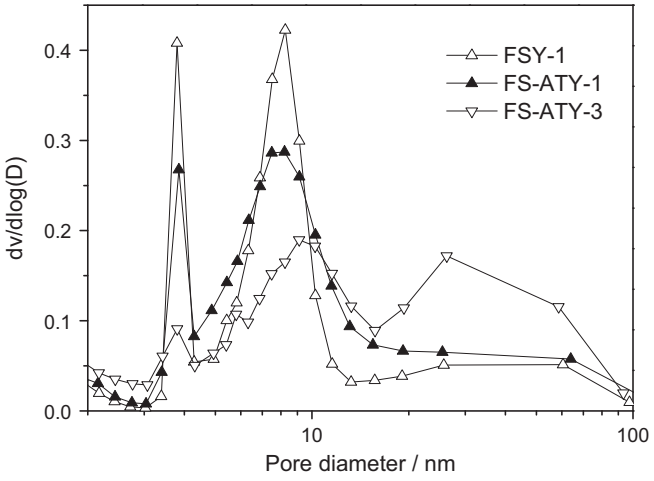

Fig. 3. Pore size distributions of the FSY-1, FS-ATY-1, and FS-ATY-3 zeolites.

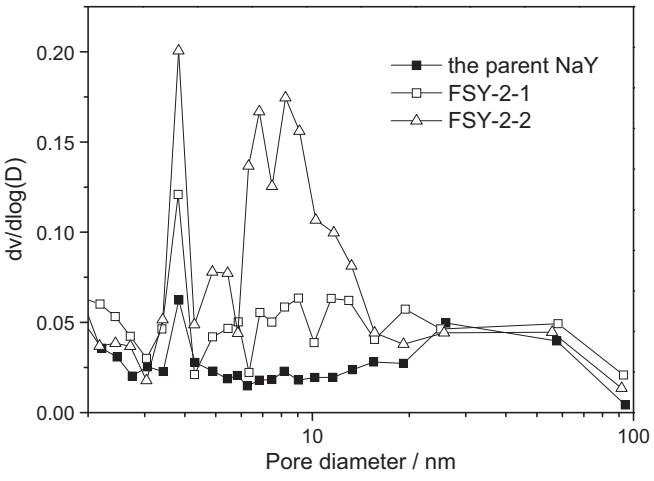

Fig. 4. Pore size distributions of the parent NaY and FSY-2–1,2 zeolites.

dealuminated samples still show a bimodal curve. In Fig. 4, two peaks whose positions closely resemble those observed for the FSY-1 zeolite are also observed for the FSY-2–2 zeolite. In the case of the FS-ATY-2–2 zeolite (Fig. 5), the positions of the two maxima in the pore size distribution are very close to those of the FS-ATY-3 zeolite.

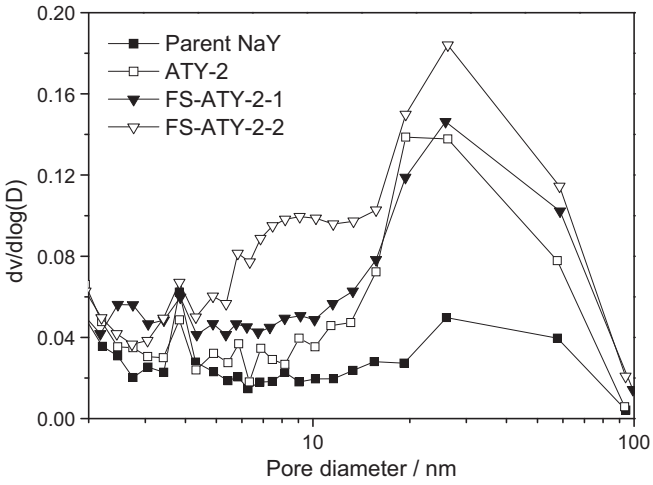

Fig. 5. Pore size distributions of the parent NaY, ATY-2, FS-ATY-2–1 and FS-ATY-2–2 zeolites.

3.2.2. TEM observation

The TEM images (Fig. 6A–H) provide us with a direct observation of the morphology of the NaOH and/or AHFS-treated samples. The crystalline region of the FSY zeolites shows no indication of mesopores (Fig. 6A–C). Only between the out surface and the main body of the crystallite there is a layer of light material (the belt-shaped zone indicated by the arrow in Fig. 6B). According to Ohsuna et al. [10,43], this layer is a result of crater formation and its further expansion. We therefore suggest that this less dense layer is responsible for the existence of the mesopores, or craters, to be exact, in these FSY zeolites as indicated by the N_2 sorption results (Section 3.2.1). The mesopores are spread all over the crystal particles of the FS-ATY zeolites under the electron beams (Fig. 6D–F). What is more, these mesopores are much more accessible to the large probe molecules than the craters in the FSY zeolites, since all the FS-ATY zeolites show both higher amounts of mercury intrusion and higher V_{Hg}/V_{meso} ratio than the FSY zeolites on a comparative basis (Table 4). Especially noteworthy is that both FS-ATY-2–2 and FS-ATY-3 zeolites show analogous V_{meso} and V_{Hg} values.

Dense material coats most parts of the FSY-1 zeolite surface (Fig. 6A and B). There is no obvious evidence that this dense layer is crystalline and crossed by observable pores (Fig. 6B). Between this and the crystalline phase, there is the much lighter layer mentioned above (Fig. 6A and B). Ohsuna et al. had already reported the co-occurrence of the dense and lighter layers [10]. They suggested

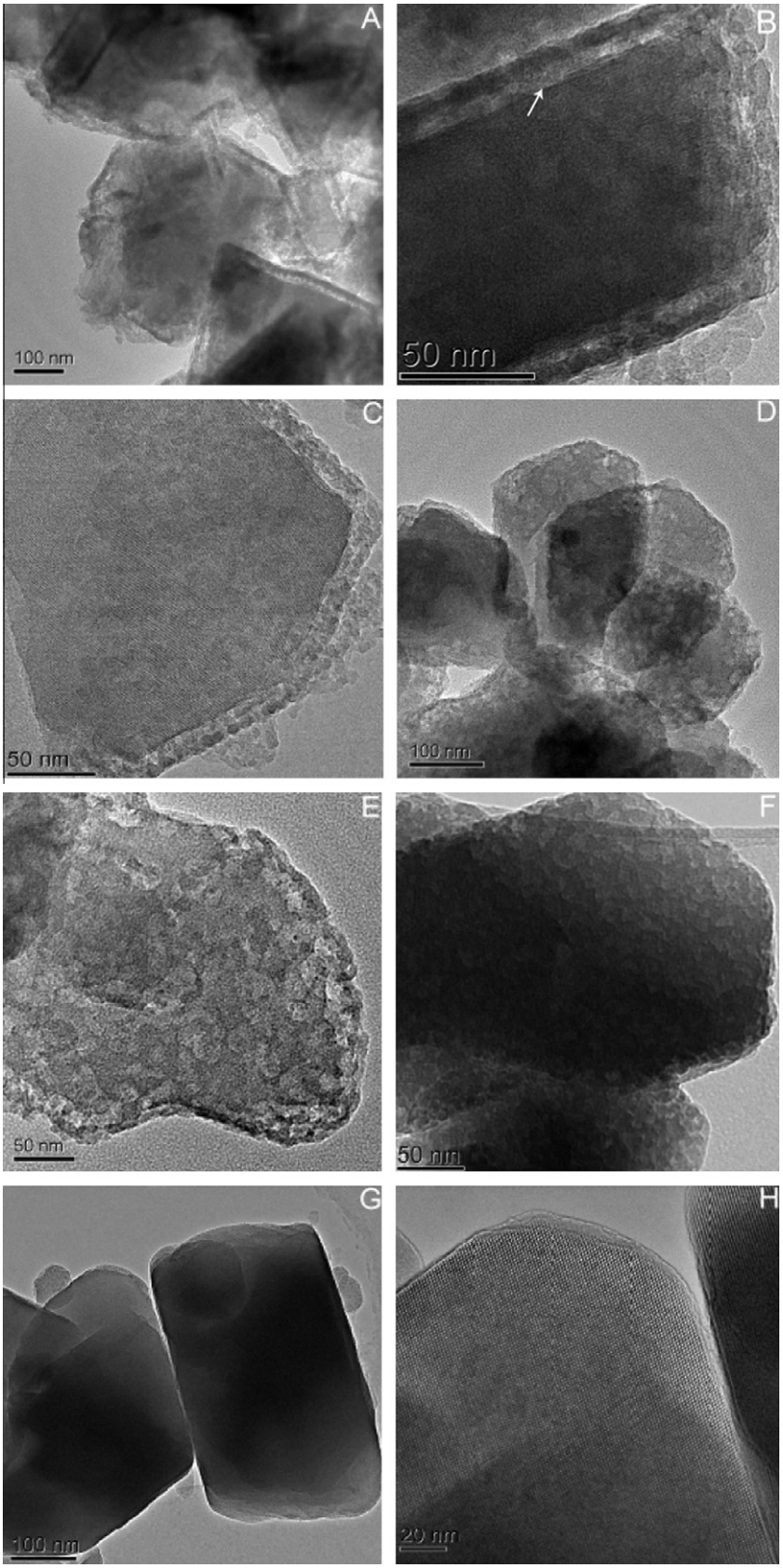

Fig. 6. A-**H**. TEM images of the FSY-1 (A, B), FSY-2–2 (C), FS-ATY-1 (D, E), FS-ATY-2–2 (F), and ATY (G, H) zeolites.

that the formation of the dense outer layer is the result of surface silica deposition, while the lighter inner layer is due to heavy local-area dealumination. It seems that this is also the case for the FSY-1 zeolite.

According to Garralón et al. [19] and Matharu et al. [42], a reduction in the reactant concentration is good for the control of the aluminum extraction. We also carried out such an experiment to measure to what extent this approach would improve the aluminum–silicon distribution of the final product. As can be seen for the FSY-2–2 zeolite, although the crystalline phase is still coated by a crust (Fig. 6C), this amorphous layer shows almost homogeneous contrast under electron beams. Since there is no sign of the existence of a lighter area, it seems that our TEM observations agree well with the conclusions of Garralón et al. [19] and Matharu et al. [42] that the dealumination uniformity can be improved if more moderate reaction conditions are used. On the other hand, the fact that the amorphous layer is still clearly visible suggests that severe silicon deposition still exists on the surface of the FSY-2–2 zeolite. This is confirmed by the fact that the surface SiO_2/Al_2O_3 ratio of this zeolite is still 13.2 higher than its bulk SiO_2/Al_2O_3 ratio (Table 3). This may suggest that the optimization of the reaction conditions improves the control of aluminum removal only moderately. It seems that the surface silicon deposition cannot be avoided by simply modifying the reaction conditions.

In the case of the FS-ATY-1 zeolite, however, both the dense outer crust and the lighter inner layer were not observed (Fig. 6D and E). Several different specimens were examined, and similar phenomena were observed. In addition, the same result is obtained for the FS-ATY-2–2 zeolite (Fig. 6F). Apparently, pre-treating the parent material with NaOH greatly improves its dealumination characteristics and the aluminum–silicon distribution of the final product. The combination of the pre-desilication and the modification of the reaction conditions works even better. The decrease in the surface SiO_2/Al_2O_3 ratio of 25.0 for the FSY-1 zeolite to 16.4 for the FS-ATY-1 zeolite (Table 3) supports these suggestions. The $(SiO_2/Al_2O_3)_{XPS}$ ratio of the FS-ATY-2–2 zeolite even decreased to 7.6, which is very close to the $(SiO_2/Al_2O_3)_{XRD}$ ratio, suggesting an almost homogeneous aluminum–silicon distribution in FS-ATY-2–2.

3.3. Catalytic activity of the FSY and FS-ATY zeolites

Differences in the acid amount of the FSY and FS-ATY zeolites are shown by the NH_3-TPD results. The FS-ATY zeolites have only slightly higher acid amounts than the corresponding FSY zeolites (Figs. 7 and 8). For the FSY-1, FSY-2–2, FS-ATY-1, and FS-ATY-2–2 zeolites, the bulk silicon-to-aluminum ratio is 10.9, 9.6, 9.6 and 8.7. If we assume that these zeolites are exempt from framework defects and non-framework aluminum species, the number of aluminum atoms in the unit cell would be about 30, 33, 33, and 36. So it is reasonable for these zeolites to show similar higher amount of acid sites, since the total acid site concentration is proportion to the aluminum concentration in a zeolite that is free of non-framework aluminum species.

Both the cracking of cumene and TIPB were investigated to compare the catalytic performance of the FS-ATY zeolites with that of the FSY zeolites and to evaluate the application potential of the sequential desilication–dealumination-modified zeolites. In the case of cumene cracking, the FS-ATY zeolites showed a higher conversion rate than the FSY zeolites between 413 and 453 K (Fig. 9). Further increasing the temperature from 453 to 493 K, however, diminished these activity differences. It is suggested that there is a higher amount of stronger acid sites in the framework of the FS-ATY zeolites than that in the FSY zeolites, which is a result of the more homogeneous dealumination of the framework of the former zeolites. As a result, the reactant molecules can be more easily activated at lower temperature when the cracking reaction is carried out on the surface of the FS-ATY zeolites. The cumene conversion rates of these zeolites grew closer as the reaction temperature increased. This can be understood by considering that the acid amounts of all the zeolites are very similar. Besides, the critical diameter of cumene (0.68 nm) is smaller than the pore opening of the Y zeolite (0.74 nm). In this condition, there is no diffusional transport constraint influencing the rate of catalytic cracking [44]. In the catalytic conversion of TIPB, the FS-ATY-type zeolites showed both higher initial activity and lower deactivation tendency than the FSY-type zeolites (Fig. 10). This is an expected phenomenon given that the critical diameter of the TIPB molecule is 0.95 nm, which is larger than the pore diameter of the Y zeolite. In this condition, the catalytic cracking of this bulk molecule on the microporous Y zeolite would be diffusion-controlled [44]. There is a higher amount of aluminum on the surface of the FS-ATY-type zeolites than on the surface of the FSY-type zeolites. Besides, the mesopores in the framework of the former zeolites are more accessible than those in the framework of the latter zeolites. Therefore, there is an increased opportunity for the TIPB molecules to be cracked on the external and mesoporous surfaces of the FS-ATY-type zeolites. Additionally, the products can diffuse out more quickly in the case of the FS-ATY-type zeolites. The chance for coke formation on these zeolites will be smaller than on FSY-type zeolites. As a result, the former zeolites exhibit lower deactivation tendency in the catalytic conversion of TIPB. These results suggest that the FS-ATY zeolites may increase the conversion efficiency as well as reduce the deactivation rate in the catalytic reaction.

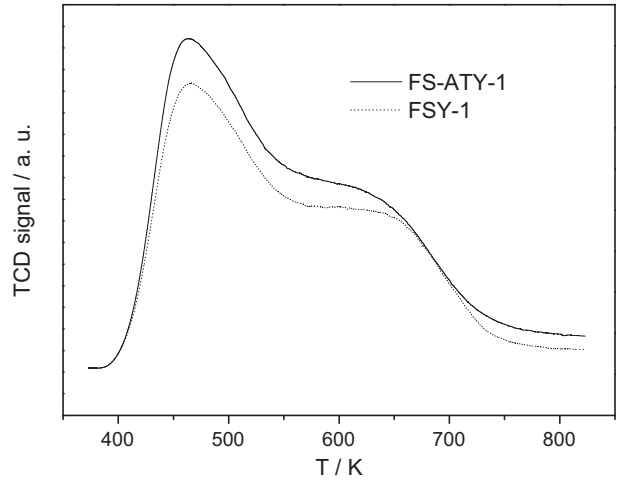

Fig. 7. NH_3-TPD profiles of the FSY-1 and FS-ATY-1 zeolites.

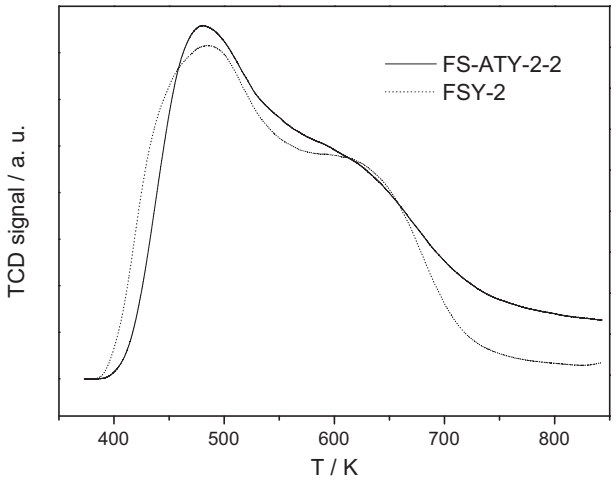

Fig. 8. NH_3-TPD profiles of the FSY-2–2 and FS-ATY-2–2 zeolites.

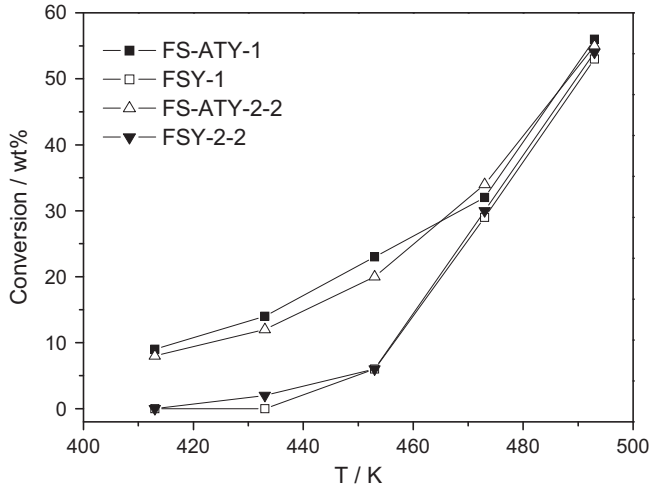

Fig. 9. Comparison of activity of FSY and FS-ATY-type zeolites for the catalytic conversion of cumene. Vaporized cumene in nitrogen (273 K) in feed, flow rate = 4.5 l h^{-1}.

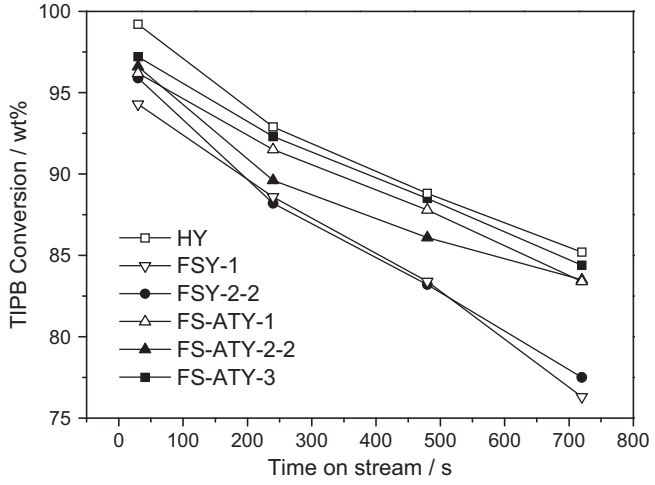

Fig. 10. Comparison of initial activity of HY-, FSY- and FS-ATY-type zeolites for the catalytic conversion of 1,3,5-triisopropylbenzene (TIPB). Vaporized TIPB in nitrogen (353 K) in feed, flow rate = 12 l h^{-1}, reaction temperature: 423 K.

The TIPB catalytic cracking performance of the starting material (HY type) is also included (Fig. 10). The HY zeolite was prepared by ion exchange of the parent NaY zeolite with ammonium chloride solutions, followed by drying at 373 K. At the beginning of the reaction, the HY zeolite showed higher conversion rate of TIPB than the FS-ATY and FSY zeolites (Fig. 10). As the reaction continued, HY zeolite showed similar activity to those FS-ATY-type zeolites, but the activity was still higher than that of the FSY-type zeolites. This is a positive sign, which indicates that the loss of activity caused by dealumination can be mitigated by the proper introduction of mesopores and the adjustment of distribution of framework aluminum.

4. Discussion

In view of earlier work [10,22–26], it is not surprising that mesopores are created in our AHFS-dealuminated zeolites. It is surprising, however, that it seems easy to create mesopores in the Y zeolite framework by AHFS treatment and that the mesopore size distribution of all the samples displays two peaks (Figs. 3–5). Our pore size distribution centered around 4 nm in diameter could be the same as the maximum near 5 nm observed by Lynch et al. [22] and could be attributed to the tensile strength effect of the N_2 molecules at $P/P_0 = 0.42$, but there is no explanation reported for the occurrence of the 8 nm peak in the pore size distributions. What makes things more complicated is that the pore size distributions centered around 4 nm in diameter gradually disappeared in the case of the FS-ATY zeolites. Furthermore, a new peak centered at around 26 nm occurred in the pore size distribution of the FS-ATY-2–1,2 and FS-ATY-3 zeolites. Obviously, the pre-desilication treatment is responsible for the occurrence of these new pores, since similar profiles were also observed in the pore size distribution of the corresponding desilicated precursors (Fig. 2). A subsequent increase in this peak intensity during the following dealumination processes is observed in Fig. 5.

The only research dealing with the distribution and morphology of the mesopores in AHFS-dealuminated zeolites was carried out by Lynch et al. [22] By combining electron microscopy and N_2 adsorption, they found that mesopores were only formed in the AHFS-treated samples when the starting zeolite had been dealuminated at least 50% [22]. This supports that mesopores can be formed in a AHFS-dealuminated zeolite but that it is not common. This is easy to understand from the mechanism of dealumination by AHFS, which is believed to proceed via the isomorphous substitution of aluminum by silicon within the zeolite framework. This mechanism implies that products having little or no aluminum vacancies can be prepared by AHFS treatment as long as the dealumination rate is under control. It suggests, however, that the zeolite framework may not preserve its integrity if the silicon insertion rate is too slow to repair the vacancies left by aluminum removal.

Based on the above discussion, we may reconsider the mesopore formation in the traditional AHFS dealumination treatment. It seems that mesopores are only formed when framework dealumination is out of control. That may be the reason why a supplementary condition of dealumination level higher than 50% has often been imposed by authors who reported the formation of mesopores in AHFS-treated zeolites [22,23]. These mesopores were directly observed, and their distribution was identified by TEM. All mesopores exist only on the subsurface of the dealuminated zeolites (Fig. 6A and B). Obviously, this kind of mesopore formation should be avoided if a crystalline sample with high surface acidity is to be obtained. Both the pre-desilication and the subsequent AHFS dealumination seem to be indispensable for the mesopore formation in the FS-ATY zeolites. Neither the single desilication nor the individual dealumination contributes to such mesopore formation, since all crystal parts of the ATY zeolite show homogeneous contrast under the electron beams (Fig. 6G and H), and there are only some craters on the surface of the FSY-type zeolites. It seems that the pre-desilication acts as an inducement for the mesopore formation by creating some defects in the framework of the ATY zeolites. The increment of the Vmeso value (Table 4) and the growth of the 26-nm peak (Fig. 2) with increasing NaOH concentration confirmed the existence of these defects. Maybe these defects are too large in size to accommodate the extraneous $Si(OH)_4$ during the AHFS treatment. As a result, they remain in existence and undergo further development with the help of the neighboring vacancies left by aluminum removal. It is highly possible that these mesopores as well as their precursors, the desilication-created defect sites, greatly facilitate the intra-crystalline transfer of the reactant molecules, thereby decreasing the concentration gradient and finally improving the aluminum–silicon distribution of the product.

With regard to the formation sequence of the amorphous materials (Fig. 6A–C), Ohsuna et al. considered that the outer layer is created first. Then some craters are formed under this layer of

amorphous material, which further expands and finally forms the lighter inner layer [10]. However, we suggest, on the contrary, that the craters form in advance of the dense outer layer. In addition, we suggest that the pore opening of the craters created under our experimental conditions is just 8 nm or so, as shown in Fig. 3. It is known that the AHFS dealumination process proceeds in two steps [1] and that the reaction rate of the second step (silicon insertion) is considerably slower than that of the first one (aluminum removal) [19]. Especially if a high SiF_6^{2-}/NH_4NaY ratio is used, the number of extracted aluminum atoms, before any silicon is inserted, will be very high [19]. Moreover, it is reported that AHFS dealumination is a diffusion-controlled reaction [7,17,18]. Therefore, it is safe to speculate that most aluminum removal reactions happen on the surface of the NH_4NaY zeolite, at least in the case of a severe AHFS dealumination process. That is why we believe that the craters of about 8 nm pore size form first, since these surface defects must be the place where intensive dealumination happened. Treating the NH_4NaY zeolite with AHFS solution of a lower concentration (Case 2) affords FSY-2–2 zeolite a weaker peak at round 8 nm in the pore size distribution than that of the FSY-1 zeolite (Figs. 3 and 4). The peak around 8 nm in the pore size distribution of the FS-ATY-2–2 zeolite almost disappears (Fig. 5). These phenomena support our proposal that the 8-nm peak is a result of intensive local-dealumination.

The boundary of the crater-region is not clearly defined until the dense outer layer is formed. This is because the intra-crystalline transport of the orthosilicic acid ($Si(OH)_4$) molecules is also diffusion-controlled. When high concentrations of $Si(OH)_4$ species are present in the liquid phase, they are easy to accumulate and gradually deposit on the outer and mesoporous defect surface of the zeolite. These surface deposits gather into a mass and then finally contribute to the dense outer layer formation. The dense layer formation markedly facilitates the visual delineation of the boundary of the crater-region, that is, the lighter inner layer that lies beneath the dense outer one under the election beams. As the surface silicon deposition becomes increasingly intense, the pore opening of many craters are partially or even entirely blocked by the silicon deposits. Then finally, these depositions contribute to the formation of ink-bottle-like mesopores that show their existence by showing a sharp peak at ca. 4 nm in the pore size distribution (Fig. 3). Now, it is easy to understand why the 4-nm peak in the pore size distributions gradually disappears in the case of the FS-ATY zeolites. It means the silicon deposition is almost totally avoided, which coincides with the XPS characterization results reported in Section 3.1.

5. Conclusions

AHFS dealumination provides Y samples with substantial surface silicon deposition, and craters of about 8 nm pore size are created on the outer surface of these dealuminated zeolites. Both are caused by the insufficient intra-crystalline diffusion of the reactant molecules. The mesoporous defects on the outer surface are partially or entirely blocked by silicon deposits. These depositions contribute to the formation of ink-bottle-like mesopores.

The combined use of sequential desilication and AHFS treatment leads to Y products with a homogeneous aluminum–silicon distribution. Upon desilication, framework silicon is extracted from the parent NaY zeolite without deteriorating zeolite crystallinity. As a result, defects of different sizes are created in the ATY zeolite. Framework defect effectively facilitates the intra-crystalline transport of reactant molecules during the following AHFS dealumination process. This increases the dealumination uniformity, and surface silicon deposition is avoided in the preparation of FS-ATY zeolites. The framework defects can coalesce and develop further into well-accessible mesoporous structures.

The FS-ATY zeolites show a higher conversion rate of cumene than the FSY zeolites between 413 and 453 K (Fig. 9). This is attributed to the more homogeneous distribution of framework aluminum in the FS-ATY zeolites, which provides the FS-ATY zeolites with a higher amount of stronger acid sites than that in the FSY zeolites. In the catalytic conversion of TIPB, the FS-ATY zeolites are more active and stable than FSY zeolites. The improved accessibility of the active sites and the reduced diffusional path lengths of the FS-ATY zeolites are probably responsible for the improvements in catalytic efficiency.

Acknowledgments

We thank Professor Xuanwen Li of Peking University for fruitful discussions and Associate Professor Yingxia Wang of Peking University for the refinement of unit cell parameters. We also acknowledge the funding of this project by MOST “973” Project of China (2010CB226904), PetroChina and NSFC (ID 20876171).

References

[1] H.K. Beyer, in: H.G. Karge, J. Weitkamp (Eds.), Molecular Sieves Science and Technology, Springer, Heidelberg, 2002, p. 203.
[2] G. Pál-Borbély, H.K. Beyer, Phys. Chem. Chem. Phys. 5 (2003) 2145.
[3] G. Pál-Borbély, H.K. Beyer, Phys. Chem. Chem. Phys. 5 (2003) 5544.
[4] J. Pires, A. Carvalho, M. Pinto, J. Rocha, J. Porous Mater. 13 (2006) 107.
[5] H.-M. Kao, P.-C. Chang, J. Phys. Chem. B 110 (2006) 19104.
[6] M.A. Zanjanchi, A. Ebrahimian, Mater. Chem. Phys. 110 (2008) 228.
[7] J.M. Cruz, A. Corma, V. Fornés, Appl. Catal. 50 (1989) 287.
[8] R. López-Fonseca, J.I. Gutiérrez-Ortiz, M.A. Gutiérrez-Ortiz, J.R. González-Velasco, J. Catal. 209 (2002) 145.
[9] B. Chauvin, M. Boulet, P. Massiani, F. Fatula, F. Figueras, T. Des Courieres, J. Catal. 126 (1990) 532.
[10] T. Ohsuna, O. Terasaki, D. Watanabe, M.W. Anderson, S.W. Carr, Chem. Mater. 6 (1994) 2201.
[11] C.S. Triantafillidis, A.G. Vlessidis, L. Nalbandian, N.P. Evmiridis, Micropor. Mesopor. Mater. 47 (2001) 369.
[12] H.-M. Kao, Y.-C. Chen, J. Phys. Chem. B 107 (2003) 3367.
[13] X. Zhu, S. Liu, Y. Song, L. Xu, Catal. Commun. 6 (2005) 742.
[14] R. Le Van Mao, G. Denes, N.T.C. Vo, J.A. Lavigne, S.T. Le, in: S. Komarneni, D.M. Smith, J.S. Beck (Eds.), Advances in Porous Materials, Mater. Res. Soc. Symp. Proc., Pittsburgh, PA, 1994, Warrendale, PA, 1995, p. 123.
[15] R.A. Rakoczy, Y. Traa, Micropor. Mesopor. Mater. 60 (2003) 69.
[16] H.-M. Kao, Y.-C. Chen, C.-C. Ting, P.T. Chen, J.-C. Jiang, Catal. Today 97 (2004) 13.
[17] J.M. Silva, M.F. Ribeiro, F. Ramôa Ribeiro, E. Benazzi, N.S. Gnep, M. Guisnet, Zeolites 16 (1996) 275.
[18] Q.L. Wang, M. Torrealba, G. Giannetto, M. Guisnet, G. Perot, M. Cahoreau, J. Caisso, Zeolites 10 (1990) 703.
[19] G. Garralón, V. Fornés, A. Corma, Zeolites 8 (1988) 268.
[20] J.A. van Bokhoven, T.-L. Lee, M. Drakopoulos, C. Lamberti, S. Thiesz, J. Zegenhagen, Nat. Mater. 7 (2008) 551.
[21] J.A. van Bokhoven, N. Danilina, in: J. Čejka, A. Corma, S. Zones (Eds.), Zeolites and Catalysis: Synthesis, Reactions and Applications, Wiley-VCH, Weinheim, 2010, p. 283.
[22] J. Lynch, F. Raatz, C. Delalande, in: K.K. Unger, J. Rouquerol, K.S.W. Sing, H. Kral (Eds.), Studies in Surface Science and Catalysis, Characterization of Porous Solids, vol. 39, Elsevier, Amsterdam, 1988, p. 547.
[23] C.S. Triantafillidis, N.P. Evmiridis, Ind. Eng. Chem. Res. 39 (2000) 3233.
[24] R. López-Fonseca, B. de Rivas, J.I. Gutiérrez-Ortiz, J.R. González-Velasco, in: F. Rodriguez-Reinoso, B. McEnaney, J. Rouquerol, K. Unger (Eds.), Studies in Surface Science and Catalysis, Characterization of Porous Solids VI, vol. 144, Elsevier, Amsterdam, 2002, p. 717.
[25] S. van Donk, A.H. Janssen, J.H. Bitter, K.P. de Jong, Cat. Rev. Sci. Eng. 45 (2003) 297.
[26] Y. Tao, H. Kanoh, L. Abrams, K. Kaneko, Chem. Rev. 106 (2006) 896.
[27] J.C. Groen, L.A.A. Peffer, J.A. Moulijn, J. Pérez-Ramírez, Micropor. Mesopor. Mater. 69 (2004) 29.
[28] X. Li, R. Prins, J.A. van Bokhoven, J. Catal. 262 (2009) 257.
[29] J.C. Groen, S. Abelló, L.A. Villaescusa, J. Pérez-Ramírez, Micropor. Mesopor. Mater. 114 (2008) 93.
[30] J.C. Groen, W. Zhu, S. Brouwer, S.J. Huynink, F. Kapteijn, J.A. Moulijn, J. Pérez-Ramírez, J. Am. Chem. Soc. 129 (2007) 355.
[31] L. Zhao, B. Shen, J. Gao, C. Xu, J. Catal. 258 (2008) 228.
[32] D. Verboekend, J.C. Groen, J. Pérez-Ramírez, Adv. Funct. Mater. 20 (2010) 1441.
[33] J.C. Groen, L.A.A. Peffer, J.A. Moulijn, J. Pérez-Ramírez, Chem. Eur. J. 11 (2005) 4983.
[34] R. Le Van Mao, S. Xiao, A. Ramsaran, J. Yao, J. Mater. Chem. 4 (1994) 605.
[35] T.K. Maji, R. Matsuda, S. Kitagawa, Nat. Mater. 6 (2007) 142.

[36] B. Shen, X. Gao, P. Zeng, B. Wang, Y. Wang, H. Liu, X. Pang, S. Qin, J. Guo, Q. Guo, J. Zheng, C. Gong, L. Zhang, J. He, C. Duan, L. Zhao, CN Patent ZL 2004 1 0097108.3, to Petrochina Company Ltd., 2004.
[37] A. Le Bail, H. Duroy, J.L. Fourquet, Mater. Res. Bull. 23 (1988) 447.
[38] D.W. Breck, Zeolite Molecular Sieves: Structure, Chemistry, and Use, New York, 1974, p. 94.
[39] D.-S. Liu, S.-L. Bao, Q.-H. Xu, Zeolites 18 (1997) 162.
[40] G. Zi, T. Yi, Zeolites 8 (1988) 232.
[41] G. Agostini, C. Lamberti, L. Palin, M. Milanesio, N. Danilina, B. Xu, M. Janousch, J.A. van Bokhoven, J. Am. Chem. Soc. 132 (2009) 667.
[42] A.P. Matharu, L.F. Gladden, S.W. Carr, in: H.K. Beyer, H.G. Karge, I. Kiricsi, J.B. Nagy (Eds.), Studies in Surface Science and Catalysis, Catalysis by Microporous Materials, vol. 94, Elsevier, Amsterdam, 1995, p. 147.
[43] O. Terasaki, T. Ohsuna, Top. Catal. 24 (2003) 13.
[44] S. Al-Khattaf, H. de Lasa, Appl. Catal. A 226 (2002) 139.